# Transient Absorption Microscopy using Widefield Lock-in Camera Imaging

Kelly S. Wilson[1], Tanner S. Volek[1], Niklas Gross[2], Stephan Link[2,3,4,5], Carlos R. Baiz[1*], & Sean T. Roberts[1*]

*[1]Department of Chemistry, The University of Texas at Austin, Austin, TX 78712, USA*
*[2]Department of Chemistry, Rice University, Houston, TX 77005, USA*
*[3]Department of Electrical and Computer Engineering, Rice University, Houston, TX 77005, USA*
*[4]Department of Chemistry, University of Illinois Urbana-Champaign, Urbana, IL 61801, USA*
*[5]Department of Electrical and Computer Engineering, University of Illinois Urbana-Champaign, Urbana, IL 61801, USA*

[*]Authors to whom correspondence should be sent: cbaiz@cm.utexas.edu & roberts@cm.utexas.edu

**Abstract:**

Over the last decade, the proliferation of pulsed laser sources with high repetition rates has facilitated a merger of ultrafast time-resolved spectroscopy with imaging microscopy. In transient absorption microscopy (TAM), the excited state dynamics of a system are tracked by measuring changes in the transmission of a focused probe pulse following photoexcitation of a sample. Typically, these experiments are done using a photodiode detector and lock-in amplifier synchronized with the laser and images highlighting spatial heterogeneity in the TAM signal are constructed by scanning the probe across a sample. Performing TAM by instead imaging a spatially-defocused widefield probe with a multipixel camera could dramatically accelerate the acquisition of spatially-resolved dynamics, yet approaches for such widefield imaging generally suffer from reduced signal-to-noise due to an incompatibility of multipixel cameras with high-frequency lock-in detection. Herein we describe implementation of a camera capable of high-frequency lock-in detection, thereby enabling widefield TAM imaging at rates matching those of high-repetition rate lasers. Transient images using a widefield probe and two separate pump pulse configurations are highlighted. In the first, a widefield probe was used to image changes in the spatial distribution of photoexcited molecules prepared by a tightly-focused pump pulse while in the second, a widefield probe detected spatial variations in photoexcited dynamics within a heterogeneous organic crystal excited by a defocused pump pulse. These results highlight the ability of high-sensitivity lock-in detection to enable widefield TAM imaging, which can be leveraged to further our understanding of excited state dynamics and excitation transport within spatially-heterogeneous systems.

## Introduction

Ultrafast spectroscopy has provided researchers with key insights into the mechanisms of chemical processes due to its ability to follow dynamics with femtosecond time resolution. While several techniques have been developed, transient absorption spectroscopy is perhaps one of the most widely applied methods for probing chemical systems. During a transient absorption experiment, a temporally short pump pulse photoexcites a sample and ensuing changes in its absorption spectrum are measured using a time-delayed probe pulse. As photogenerated species typically show distinct absorption spectra, by measuring the time-evolution of different absorption features induced by the pump, information regarding dynamic and chemical processes initiated by light can be tracked as a function of time. Detection of pump-induced changes in the transmission of a probe pulse ($\Delta T$) is typically achieved by continuously modulating the intensity of the pump using either a mechanical chopper or acousto-optic modulator (AOM). High signal-to-noise in the detection of these changes is then provided by a lock-in amplifier, which isolates the signal components that match the modulation frequency of the pump pulse train.

Over the last decade, high-power ultrafast lasers with pulse generation frequencies in the range of hundreds of kilohertz to megahertz have gained prominence due to their high pulse-to-pulse stability and faster acquisition rates.[1–3] These high repetition rate sources have enabled ultrafast science to push into the area of time-resolved microscopy.[4–8] In a transient absorption microscopy (TAM) experiment, the pump and probe pulses are focused using a high numerical aperture objective to a waist size approaching the diffraction limit. While signals measured in a TAM experiment are typically weaker than those recorded in an ensemble transient absorption measurement due to the lower pulse energies required and smaller volume of molecules being probed, this issue can be offset by the high laser repetition rate, which can allow for the isolation

of weak signals through averaging. This averaging is often performed using a lock-in amplifier due to its ability to detect signals at frequencies that match the modulation rate of the pump pulse train. Indeed, TAM studies employing lock-in detection have provided key insights into carrier transport in 2D materials,[5,9–12] energy transport in quantum dots[13–15] and molecular assemblies,[16–18] and singlet fission dynamics in molecular crystals.[19–25]

However, while commercial lock-in amplifiers can be readily used for single-channel detection, challenges arise in applications requiring multi-channel data acquisition. This limitation is evident in spectrally or spatially resolved measurements, such as broadband pump-probe spectroscopy and widefield pump-probe microscopy. The frame rate of array detectors and cameras typically employed for multichannel detection cannot match the hundreds of kilohertz to megahertz repetition rates of emerging laser systems used for ultrafast spectroscopy and microscopy, limiting some benefits these high repetition rate systems provide. While schemes for multi-channel lock-in detection have successfully been employed for ultrafast spectroscopy,[26,27] these approaches often present several challenges, such as limitations in the number of acquisition channels resulting in low spectral/spatial resolution, complex electronic triggering schemes, limited repetition frequencies, and/or challenging implementation of detectors. As a result, multi-channel lock-in detection schemes are rare within the ultrafast community.

In this report, we describe the design of a transient absorption microscope that performs widefield pump-probe imaging using a camera (Heliotis AG, Helicam C3) wherein each pixel functions as a lock-in amplifier. This camera enables multi-channel, spatially encoded lock-in detection without a complex setup needed by other multi-channel lock-in amplification solutions. The lock-in camera has previously been employed as a widefield interferometer for portable profilometry,[28] Doppler velocimetry,[29] and non-line-of-sight imaging,[30] and has been used to map

modulated changes in the fluorescence of nitrogen vacancies induced by electromagnetic fields.[31,32] Seo and coworkers employed an earlier model of the lock-in camera to perform widefield pump-probe measurements of patterned semiconductor thin films and silicon nanowires.[33] Herein, we expand on their work by both developing a widefield imaging scheme that allows $\Delta T/T$ signals to be directly acquired using quadrature detection and demonstrate two widefield imaging modes wherein the focal size of the pump pulse is varied. In the first mode, the pump is tightly focused, which produces a localized excitation whose spatial migration over time can be visualized via a spatially defocused probe. In the second mode, the pump and probe are both defocused, enabling widefield transient imaging to assess how different heterogeneous regions of a sample impact its photoexcited dynamics. As a model system for demonstrating these imaging modes, we employ single crystals of N,N′-bis(2-phenylethyl)-3,4,9,10-perylenedicarboximide (EP-PDI), an organic singlet fission material[34,35] that is currently of interest for applications in light harvesting.[36] Our work demonstrates the versatility of lock-in imaging for ultrafast microscopy, which can enable new discoveries in nanoscience, biology, and materials science.

## Methods

**EP-PDI Crystal Growth.** Following a similar procedure outlined by Kim and coworkers,[37] self-assembled EP-PDI crystals were grown from a saturated toluene solution heated to 90 °C. Separate 1-mL aliquots of the heated solution were drop cast onto deionized water. As the toluene evaporates, EP-PDI crystals form on the surface of the water solution over the course of twenty minutes. Controlling the temperature of the water bath during crystal formation can be used to control resulting EP-PDI crystal size. Large crystals with a width >10 μm and lengths ranging from 100 - 200 μm were grown by drop casting toluene onto a water bath heated to 40 ºC

that was allowed to slowly cool to room temperature over the course of one hour. Small crystals with 1-3 μm feature sizes were prepared by drop casting toluene onto water held at ambient temperature. After formation, the crystals were transferred to either a silver mirror or a glass slide for spectroscopic measurements. TAM images of large and small EP-PDI crystals were acquired with a widefield probe following excitation by a tightly focused pump or a widefield pump, respectively, as described below.

**Widefield Transient Absorption Microscope.** The sample plane of a custom-built transient absorption microscope was imaged by two cameras, a color CMOS camera (Thorlabs, CS165CU) and a lock-in camera (Heliotis AG, Helicam C3), through a 100× objective (Nikon, MPlanAPOHR, 100×/0.90 NA) as shown in **Figure 1A**. A 90:10 (reflection:transmission) beamsplitter enabled both cameras to image the sample simultaneously with the CMOS and lock-in cameras in the transmission and reflection arms, respectively. The CMOS camera, equipped with an infinity focused achromatic lens ($f$ = 200 mm), collected optical microscopy images and aided in aligning the pump, probe, sample, and lock-in camera field of view. The lock-in camera imaged the sample plane through a compound microscope for widefield transient images. Lock-in detection was performed at each pixel in a 300 × 300 array. Details of the lock-in detection scheme are described below. An achromatic tube lens ($f$ = 200 mm) created a conjugate imaging plane of the sample in front of a 40× refractive objective (Nikon PlanFluorELWD 40×/0.60 NA) whose aperture was positioned ~2 in. from the detector. That conjugate plane was imaged through the objective onto the detector, yielding a total magnification factor of ~1390× with a conversion ratio of 28.5 nm/pixel and an 8.55 × 8.55 μm field of view. The focus of the optical system was controlled by a piezo objective positioner (Newport, NPO140SG) attached to the 100× objective. An xy piezo stage (Newport, NPXY200SG or Physik Instrumente, P-517.3CL) and an xy

micrometer stage (Newport, 406) controlled the lateral position of the sample.

The transient absorption microscope was deployed in two separate laser systems with high repetition rate lasers. The first laser system was a 1 MHz, 360 fs, 1030 nm ytterbium fiber laser (Spectra-Physics, Spirit 100). An internal AOM was used to downmodulate the repetition rate to a subharmonic of the fundamental rate. The second optical setup employed a 200 kHz, 160 fs, 800 nm Ti:sapphire laser (Coherent, RegA 9000). The repetition rate for each measurement is highlighted in the Results and Discussion section. Other details of each optical setup are provided in the **Supporting Information**. Briefly, a beamsplitter divided each laser source into separate pump and probe paths. Through a combination of nonlinear optical processes and optical filters, the pump and probe were spectrally tuned to be resonant with the sample absorption profile and target spectral features in the transient signal. The pump and probe were both modulated by AOMs according to the scheme described in the lock-in camera acquisition description below. A delay stage (Newport, DLS325) controlled the pump-probe time delay before both beams were directed into the microscope.

The pump and probe can each be directed into the microscope and imaged by the cameras either in reflection or transmission, as shown in **Figure 1A**. These configurable modes enable focused and widefield pump transient imaging for both transmissive and reflective samples. Local pump transient imaging (**Figure 1B**) was achieved by focusing the pump using the 100× objective to the diffraction limit on the sample plane. For widefield pump imaging (**Figure 1C**) in reflection mode, a lens ($f$ = 1000 mm) focused the pump onto the back aperture of the objective, resulting in even illumination across the field of view at the sample. In transmission mode, an objective (Achromatic 10×/0.30 NA or Nikon PlanFluorELWD 40×/0.60 NA) with a lower numerical aperture (NA) focused the pump onto the imaging plane. The illumination region area could be

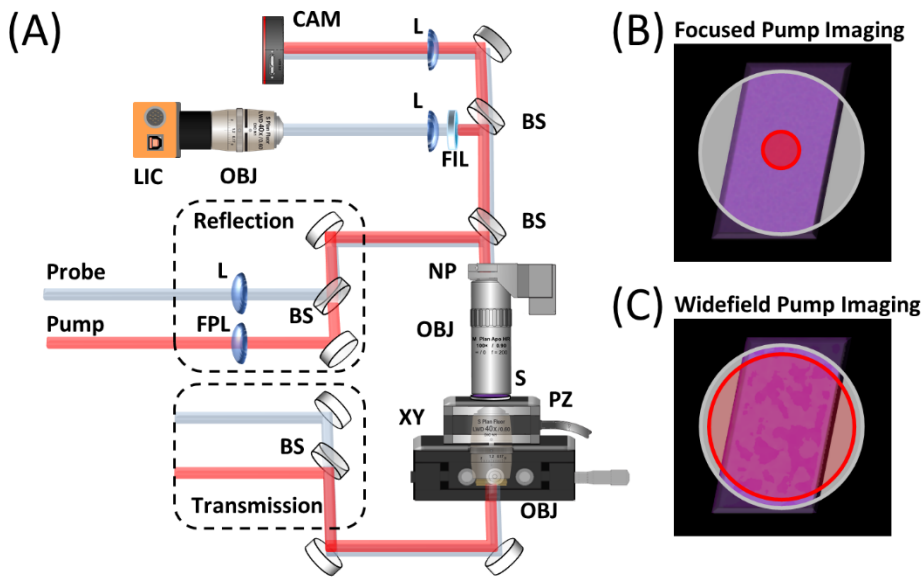


**Figure 1:** (A) TAM microscope schematic, showing reflection and transmission geometries. BS, beamsplitter; CAM, color CMOS camera; FIL, spectral filter; FPL, widefield pump lens; L, lens; LIC, lock-in camera; NP, objective nanopositioner; OBJ, objective; PZ, piezo stage; S, sample; XY, xy translation stage. Both geometries can be configured for widefield probe imaging with (B) focused and (C) widefield pump excitation.

controlled by moving the low NA objective out of focus with the imaging plane. Widefield illumination of the sample by the probe was achieved in a manner similar to the pump according to the imaging mode. Pump and probe were co-aligned with a 50:50 beam combiner and co-propagated in reflection mode and widefield pump transmission mode. A 50:50 beamsplitter routed the beams into the imaging path of the microscope when operating in reflection mode. In transmission mode using a focused pump, the pump and probe counter-propagated through the microscope, with the pump and probe travelling the reflection and transmission paths, respectively. An optical filter blocked the pump before the lock-in camera tube lens.

**Lock-in Camera Acquisition Scheme. Figure 2** shows the image acquisition scheme used for lock-in detection. The lock-in camera collects four frames per reference wave cycle that are differenced to produce an in-phase signal and quadrature signal (**Figure 2A**). The in-phase signal (blue, frames *1* and *3*) is generated by differencing images collected at the peak (frame *1*) and

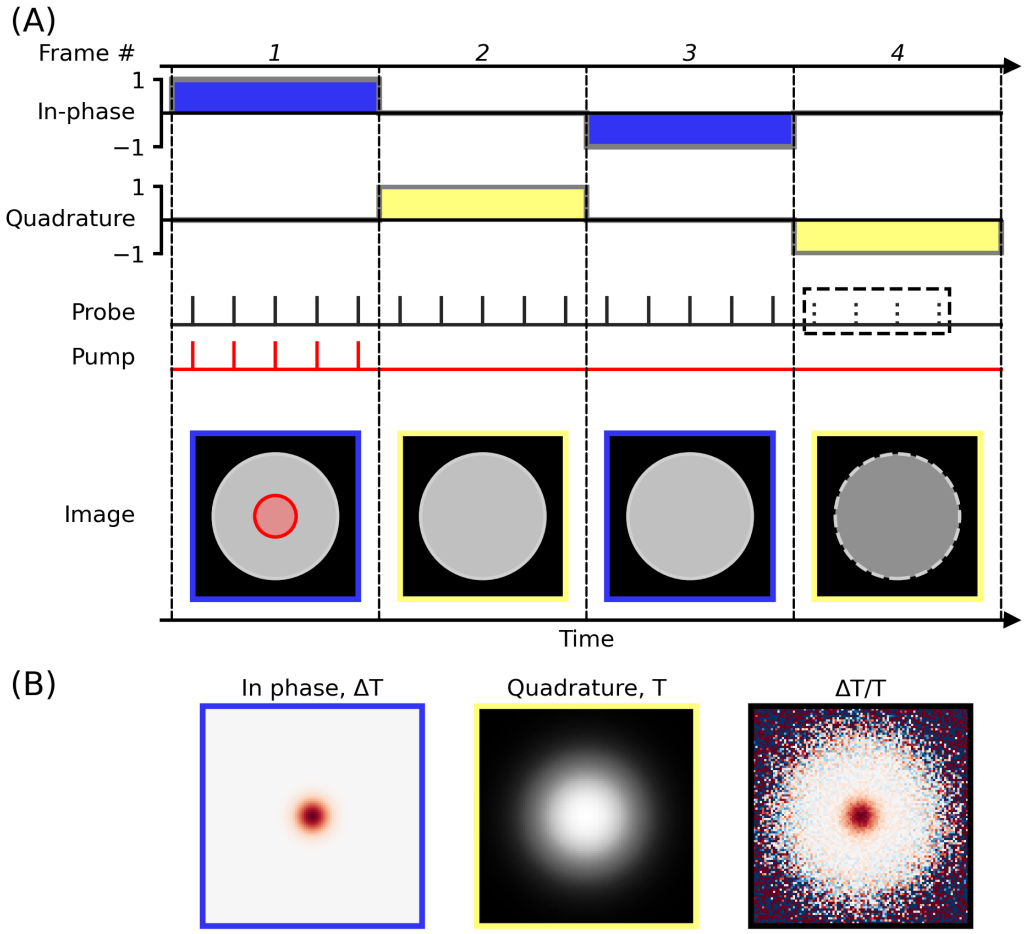


**Figure 2:** Triggering scheme for lock-in imaging of transient signals. (A) One reference cycle of the lock-in camera, separated into four frames (*1-4*). In-phase (blue) and quadrature (yellow) reference waves determine the sign of the image acquired in each frame during integration. Probe (black) and pump (red) pulses are present for frames *1-3* and *1*, respectively. Probe pulses are optional in frame *4* (dashed). Images denoting the presence of the probe (grey) or pump (red) in each period. (B) In-phase (blue), quadrature (yellow), and transient images ($\Delta T/T$) acquired after integration.

minimum (frame *3*) of the reference wave. The images acquired and differenced to produce the quadrature signal (yellow, frames *2* and *4*) are shifted by a quarter cycle from those used to produce the in-phase signal. The integration period of the lock-in detection is set by the number of reference wave cycles used to generate a lock-in image. Here, the integration period was set to 30 cycles for the data presented below. The reference frequency can be downmodulated to bin several laser pulses into each frame. This approach enables the use of low-energy pump and probe pulses that

prevent laser-induced sample damage while maintaining signal intensities on the detector that are large relative to the read noise associated with digitizing images. For the data reported herein, the number of pulses per frame ranged from 15 to 30.

Collection of a TAM image requires measuring two quantities, $\Delta T$, the change in the probe transmission induced by the pump, as well as $T$, the probe transmission in the absence of the pump. Dividing $\Delta T$ by $T$ normalizes out signal contributions that stem from spatial nonuniformity of the probe. We employ the in-phase difference signal and quadrature difference signal to collect $\Delta T$ and $T$, respectively. In typical lock-in detection, the in-phase and quadrature signals are used to acquire the amplitude and phase of a single incoming signal. To acquire both $\Delta T$ and $T$ signals simultaneously with the lock-in camera, the camera is phase synchronized with the AOMs modulating the pump and probe to align $\Delta T$ and $T$ to the in-phase and quadrature channels. Instead of considering the in-phase and quadrature channels to be two separate measurements of the same signal, they should be regarded as two separate signals, enabling division to calculate $\Delta T/T$.

Images *1* - *4* in **Figure 2A** highlight which beams are present and which reference wave is used during integration to produce frames *1* - *4*. To produce the $\Delta T$ signal, an AOM modulates the pump such that it is only present during the acquisition of frame *1* (**Figure 2A**, red) while the probe is present during frames *1* and *3*. Differencing these frames produces the $\Delta T$ signal in the in-phase image channel. To collect the $T$ signal, a second AOM modulates the probe such that the number of laser shots that contribute to frames *2* and *4* differ, with a smaller number of shots being included in frame *4* (**Figure 2A**, black). Differencing these frames yields the transmission of the probe, $T$, in the quadrature image channel. We note that a finite number of shots are collected in frame *4* to prevent saturation of the $T$ image. This saturation is not caused by an individual frame within a cycle, but rather by saturating the accumulated lock-in image acquired by integrating over several

frames. The $\Delta T$ channel (frames *1* and *3*) does not experience this issue as the probe intensity in frame *3* negates probe intensity in frame *1* during integration. However, if the probe is blocked during frame *4*, then during integration the $T$ channel can quickly saturate as the probe intensity in frame *2* would not be negated by signal in frame *4*. By introducing a limited number of probe shots in frame *4*, less than the number of shots in frame *2*, the total accumulated intensity in $T$ can be lowered below saturation while still capturing the intensity and profile of the probe. A scaling factor determined by the ratio of shots in frames *2* and *4* can then be used after collection to rescale $T$ to the appropriate intensity. **Figure 2B** shows simulated images highlighting the $\Delta T$ and $T$ lock-in images produced by this measurement scheme. The normalized TAM signal, $\Delta T/T$, is calculated by dividing these two images (**Figure 2B**, right panel). This acquisition scheme maximizes the sensitivity of the transient signal in $\Delta T$ and enables acquisition of the normalized transient image $\Delta T/T$ while avoiding saturation during lock-in imaging of the probe profile.

The lock-in camera returns unsigned 10-bit format (0 - 1023 counts) images with the lock-in baseline approximately centered in the middle of the range (500 - 600 counts), which varies pixel by pixel. To shift the baseline to zero, a baseline image must be collected for both $\Delta T$ and $T$ as they are different. Briefly, the baseline for $\Delta T$ is collected with the pump blocked while exposing the probe to the detector while the baseline for $T$ is collected with both beams blocked. Instability in the baseline over time requires a synchronous acquisition of the baseline concomitantly with the transient signal. Details of the baseline acquisition and subtraction methods are outlined in the **Supporting Information**.

The lock-in camera is capable of a maximum reference wave frequency of 250 kHz (an internal framerate of 1 MHz). The following trigger scheme was used to trigger the lock-in camera and AOMs used for the pump and probe. A digital delay pulse generator (Berkeley Nucleonics,

Model 525) was triggered at the repetition rate of the laser. A second pulse generator (Berkeley Nucleonics, Model 525) was triggered by the first at a subharmonic of the laser repetition rate and determined both the reference frequency of the lock-in camera and total number of laser shots per imaging cycle. The lock-in camera anticipates two square pulses per cycle, where the rising edge of each pulse triggers frames *1* and *3* and the falling edge triggers frames *2* and *4*. The timing of two internal channels on the pulse generator was set to generate the two pulses per cycle. The internal channels were multiplexed to a single output channel that triggered the lock-in camera. A separate channel was connected to the pump AOM and timed such that the pump was on during frame *1*. Another channel triggered the probe AOM such that the probe was on during frames *1* - *3*. For some of the measurements reported below, the timing was also set to include some probe shots in frame *4* to avoid saturation in *T*. The repetition rate and reference frequency for each of the measurements below is highlighted at the beginning of its section.

**Results & Discussion**

Transient images of an EP-PDI crystal on a silver mirror pumped at 560 nm and probed at 650 nm using the first laser system and the lock-in camera in reflection mode are shown in **Figure 3**. The repetition rate of the laser was downmodulated by the internal AOM from 1 MHz to 333 kHz. The reference frequency of the lock-in camera was set to 2.78 kHz (11.1 kHz framerate, 30 pulses/frame). Data were averaged for 30 seconds. For these measurements, the pump is focused onto the sample (FWHM, 630 nm) while the probe is defocused (FWHM, 2 μm). With this configuration, the spatially localized excited state population generated by the pump can be contrasted with the surrounding ground state population within a single image. This result is observed in the in-phase image, which shows an excited state absorption feature in the transient signal, $\Delta T$, of the EP-PDI crystal at a pump-probe time delay of 5 ps (**Figure 3A**). The widefield

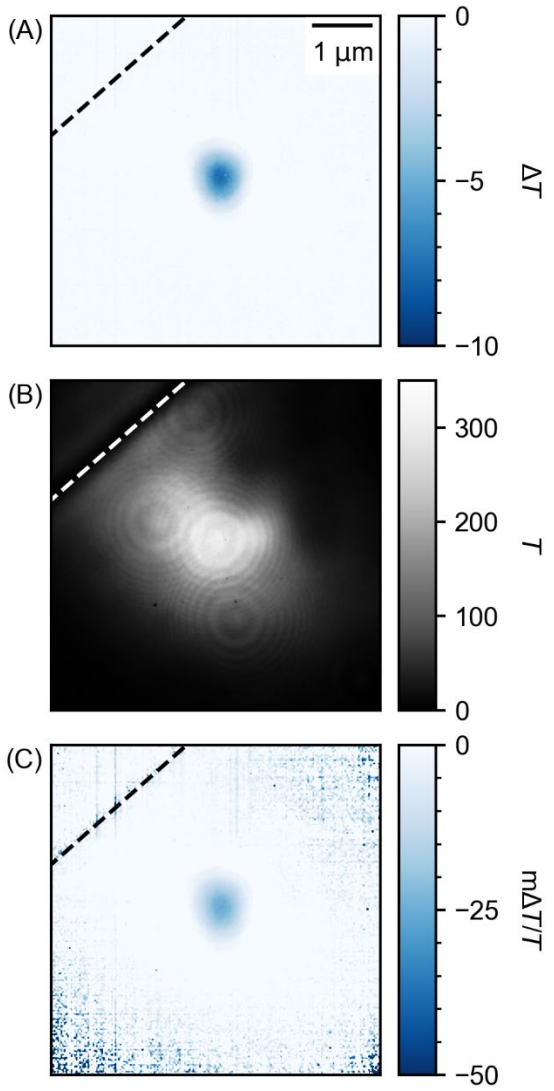


**Figure 3:** (A) In-phase ($\Delta T$), (B) quadrature ($T$), and (C) normalized TAM ($m\Delta T/T$) images of an EP-PDI crystal acquired with the lock-in camera. The dashed line marks the crystal edge. These images were acquired using a pump pulse focused close to the diffraction limit and a defocused probe pulse at a time delay of 5 ps ($\lambda_{pump}$ = 560 nm, $\lambda_{probe}$ = 650 nm).

image of the probe intensity profile, $T$, collected as the quadrature image is shown in **Figure 3B**. The probe is large enough to illuminate a portion of the sample including the edge of the PDI crystal, visible in the upper left corner of the image. Diffraction rings within the image arise from out of focus dust in the imaging setup and do not impact the normalized transient signal, $\Delta T/T$ (**Figure 3C**), which is calculated by dividing the in-phase image by the quadrature image. This normalization removes any impact of the probe spatial intensity profile on the measured signal

profile.

While noise can arise from sources such as laser instability, pixel readout noise ($\sigma_{pixel}$) dominates for the lock-in camera. This readout noise can be determined for each pixel by calculating its standard error from a sequence of lock-in images. Noise for individual pixels is also well approximated by calculating the standard deviation of a region of pixels in an averaged transient image at a baseline signal level. Noise fluctuations from the same pixel from the in-phase and quadrature images are not correlated and cannot, therefore, be used for correcting noise between both images. However, $\sigma_{pixel}$ is the same for both lock-in images. The estimated noise for a pixel in the normalized transient absorption image, $\sigma_{\Delta T/T}$, is calculated using Eq. 1:

$$\sigma_{\Delta T/T} = \left(\frac{\Delta T}{T}\right)\left(\frac{\sigma_{pixel}}{\Delta T} + \frac{\sigma_{pixel}}{T}\right) \quad (1)$$

which, with the condition that $\Delta T/T \ll 1$, can be approximated with Eq. 2:

$$\sigma_{\Delta T/T} \approx \frac{\sigma_{pixel}}{T} \quad (2)$$

Thus, the noise level for each pixel in $\Delta T/T$ is primarily dependent on the intensity of the probe in the quadrature image, *T*, within the dynamic range of the detector. This is evident in **Figure 3C**, where regions of low probe intensity around the edges of the transient image shown in **Figure 3B** manifest higher pixel noise.

The pixel noise level is calculated from a baseline region of the in-phase image shown in **Figure 3A**. This transient image is a composite from 30 seconds of averaging and results in a noise level of $\sigma_{pixel}$ = 0.15 counts. With an approximate probe intensity of 200 counts at the pump location, $\sigma_{\Delta T/T}$ for each pixel is $7.5 \times 10^{-4}\ \Delta T/T$. This level of sensitivity is on par with previous reported widefield transient measurements.[23,38] However, this value falls below that achievable using a single photodiode, standard lock-in amplifier, and an averaging period of a few seconds at a single position, which can yield sensitivities ranging from $10^{-5}$ to $10^{-7}\ \Delta T/T$.[1,39] While the

sensitivity level of a single pixel within the lock-in camera is lower, the advantage of collecting a 300 × 300 pixel field-of-view provides a significant reduction in acquisition time. Sensitivity can be increased either by employing a longer averaging period or increasing the probe intensity. Note, when increasing sensitivity by adjusting the probe intensity, care must be taken as undesired signal effects, such as cross-phase modulation or other coherent artifacts, can be caused by setting the intensity of the probe close to that of the pump. The contrast-to-noise ratio (CNR) characterizes the relationship between the signal level and the noise of a system and is calculated as CNR = $A/\sigma_{pixel}$ where $A$ is the amplitude of the signal.[40] It is dependent on pump power, sample properties, and time delay. The CNR for the transient image shown in **Figure 3C** is ~33.

Transient imaging using a focused pump pulse enables observation of the spatial distribution of photoexcited species. By scanning the delay between the pump and probe, time-dependent changes in this spatial distribution can be imaged.[5,8,18,23,38,39,41,42] To demonstrate the lock-in camera's ability to track photoexcitations, transient transmission images of a large EP-PDI crystal on a glass slide were produced using focused pump pulses at 450 nm and widefield probe pulses at 600 nm generated by the first laser system (**Figure 4**). The laser repetition rate was 1 MHz and the reference frequency of the lock-in camera was set to 10 kHz (40 kHz framerate, 25 pulses/frame). Data were averaged for 30 seconds at each time delay. The pump was focused tightly (FWHM, 430 nm) onto the sample using the 100× objective. The probe, counter propagating with respect to the pump through the sample, was loosely focused (FWHM, 9 μm) by the 10× objective and imaged through the microscope onto the lock-in camera.

**Figure 4A** shows transient images of the EP-PDI crystal recorded at different pump-probe delay times. Each image is normalized to the peak signal at 3 ps with the normalization factor shown in the image. At each time delay, the center portion of the signal is dominated by a positive

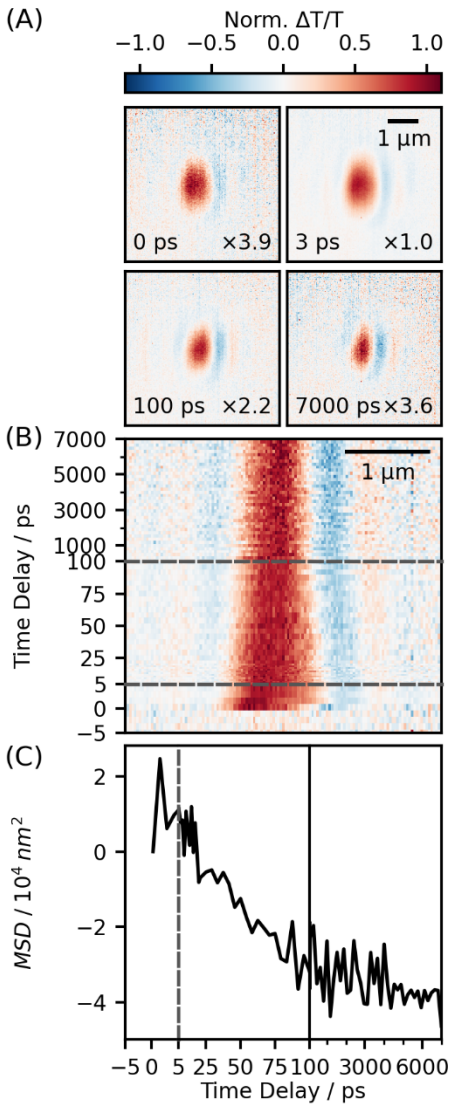


**Figure 4:** (A) Widefield TAM images taken at the center of an EP-PDI crystal at time delays of 0, 3, 100, and 7000 ps following excitation by a focused pump pulse ($\lambda_{exc}$ = 450 nm, $\lambda_{probe}$ = 600 nm). Each TAM image is normalized by the factor shown in its lower right corner. (B) Normalized horizontal cross sections of the TAM images highlighted in (A). The plotted data was produced from 80 TAM images recorded from time delays stemming from -5 ps to 7 ns. (C) MSD of the cross sections in (B) as a function of time delay. Note, the spacing of the time axes in (B) and (C) shift at 5 ps and 100 ps (dashed lines).

$\Delta T/T$ signal that we attribute to the ground state bleach associated with excitons produced within the EP-PDI crystal. Surrounding this center portion is a weak negative $\Delta T/T$ signal that arises from a photo-induced change in the crystal refractive index that alters the path of the probe as it transmits through the sample. This phenomenon has previously been discussed in detail by Ashoka

and coworkers and can be accounted for when modeling the spatial migration of photoexcited species by treating the negative signal as a part of the point spread function of the microscope.[22]

The horizontal cross sections from the normalized signal over a time delay range from 0 to 7 ns plotted in **Figure 4B** illustrate that over time the spatial width of the bleaching signal narrows. To quantify this narrowing, we fit each recorded TAM image to a 2D Gaussian model. **Figure 4C** plots the mean squared displacement (MSD) of this signal, which was calculated as the difference between the variance of the signal at each time delay, $\sigma_t^2$, and the variance of the signal at time zero, $\sigma_0^2$, along the horizontal axis. We find that the MSD rapidly expands from 0 to 3 ps after which it narrows for 100 ps. We note that rapid expansion of the spatial distribution of excitons followed by a contraction of this spatial distribution has previously been reported for tetracene,[43] a singlet fission material whose electronic structure is similar to that of EP-PDI. This contraction arises from equilibration of the singlet and triplet exciton populations involved in singlet fission. While construction of a full model of the exciton kinetics shown in **Figure 4** is beyond the scope of this work, this data demonstrates that the lock-in camera can track changes in the spatial distribution of photoexcited species over time.

To further characterize the lock-in camera's ability to quantify rates for the spatial diffusion of photoexcited species, we note a recent article published by Thiebes and Grumstrup that details how parameters such as the CNR, number of measured time points, spatial resolution, and excited state lifetime impact the accurate measurement of diffusion rates.[40] We employed a Python package developed by these authors that can be parameterized to match the experimental conditions of a transient imaging microscope to determine its precision and accuracy.[40] Spatial calibration of the lock-in camera indicates a resolution of 28.5 nm/pixel. As inputs we specify a viewing window of 3.7 μm over 130 pixels with a signal FWHM of 627 nm over 22 pixels. The

input CNR was set to 33, as determined above. A decay constant of 100 ps and a diffusion length of 30 nm were set as sample parameters. In total, 80 pump-probe time delays were acquired to match the data set shown in **Figure 4**. The proportion of simulated data sets whose fit diffusion constant was within 50% of the nominal diffusion constant (30 nm) was 0.69. This value rose to 0.98 for a nominal diffusion constant of 50 nm. These length scales are on par with measured diffusion lengths in organic electron donor and acceptor materials.[44] We note that further improvements in resolution can be gained by increasing the CNR and oversampling in the time domain.

Often microscopic-scale structural and morphological heterogeneity like crystalline grain boundaries and spot defects can have a significant influence on the bulk properties of a material.[45-49] Widefield TAM enables imaging of spatially dependent phenomena such as charge transfer, energy transport, and exciton dynamics at the sub-micron scale, without the need to carry out point-by point scanning, reducing the total acquisition time for a field of view from hours to minutes. We demonstrate widefield transient imaging of a smaller EP-PDI crystal on a glass slide using the lock-in camera and the second laser system (**Figure 5**). The laser repetition rate was 200 kHz and the reference frequency of the lock-in camera was set to 3.33 kHz (13.33 kHz framerate, 15 pulses/frame). Data were averaged for 30 seconds at each time delay. Rather than employing a tightly focused pump, the pump was defocused to photoexcite the entire region imaged by the probe in order to detect spatial variations in the transient signal across the crystal. For these measurements, a 400-nm pump pulse was used to photoexcite the sample, producing spin-singlet excitons that subsequently undergo singlet fission. This process was monitored using a probe pulse centered at 750 nm that tracked changes in the intensity of an induced absorption band associated with photogenerated singlet excitons.[34,35,50]

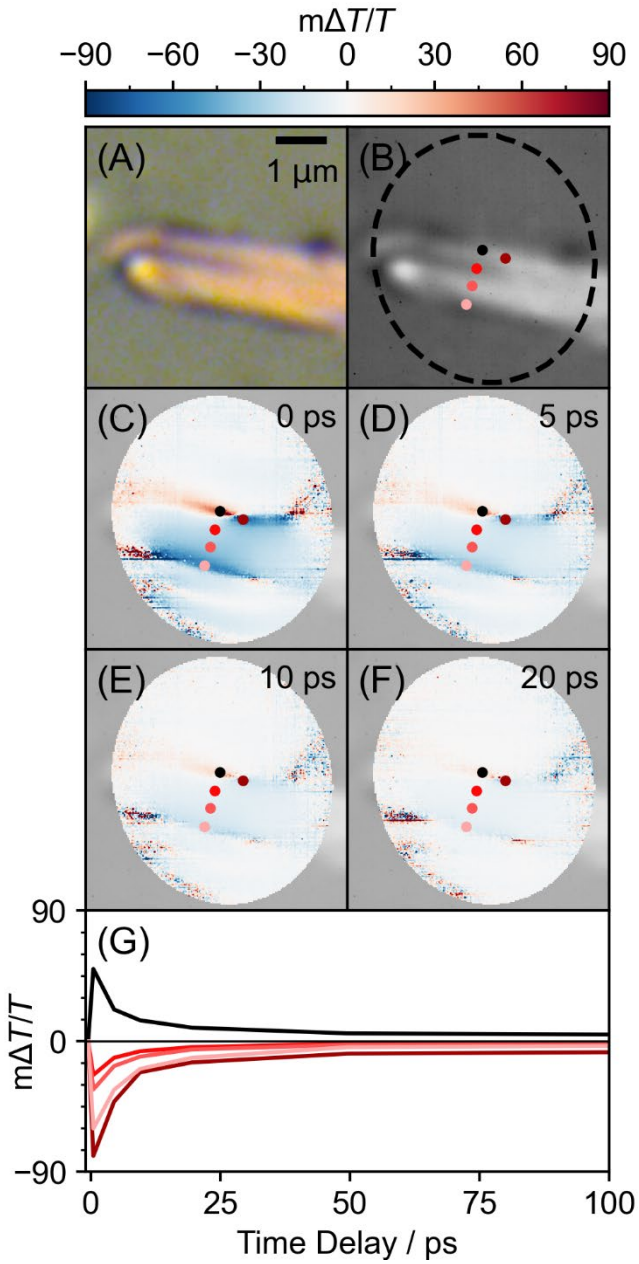


**Figure 5:** Widefield TAM images of an EP-PDI crystal collected using defocused pump and probe pulses ($\lambda_{exc}$ = 400 nm, $\lambda_{probe}$ = 750 nm). (A) Color image of the crystal recorded using a CMOS camera. (B) Image of the crystal recorded using the lock-in camera in standard imaging mode. (C-F) TAM images recorded at time delays of 0, 5, 10, and 20 ps. (G) Transients collected at spatial locations marked by circles in (B-F).

**Figure 5A** shows a color image of the crystal collected from a CMOS camera while **Figure 5B** displays an image of the crystal collected by the lock-in camera in normal imaging mode. Both images were collected in reflection mode. For the transient measurements, the probe was imaged

on the lock-in camera after transmitting through the sample. Transient images recorded at time delays of 0, 5, 10, and 20 ps are shown in **Figures 5C - 5F**. Each image was averaged for 30 seconds. A dashed line in **Figure 5B** denotes the region where the probe intensity was sufficiently high to resolve the transient signal. **Figure 5G** highlights transient dynamics measured at specific locations across the crystal denoted by dots in **Figures 5B - 5F**.

It is evident in the transient images that there is an enhancement of the signal near the edges of the EP-PDI crystal. This enhancement may be caused by a disrupted assembly of the EP-PDI molecules where the structural constraints found in the bulk of the crystal are relaxed, leading to different intermolecular electronic couplings and ultimately different singlet fission dynamics. Indeed, differences in the rate of singlet fission that occurs at the edges and in the bulk of molecular crystals have been reported. For example, distortions to the crystalline packing of molecules at the edges of TIPS-pentacene crystals have been shown to accelerate their ability to undergo SF.[25] It has also been shown that singlet fission can be enhanced near the edges of rubrene crystals due to the introduction of structural disorder that lowers the symmetry of the crystal.[24] We note that EP-PDI exhibits polymorphism,[51] which suggests unique structures could be formed at EP-PDI crystal edges that may impact their dynamics. This scenario could not only be responsible for the differences in dynamics observed within the bulk and at the edge of the crystal, but may also explain the change in the sign of the signal near the top portion of the crystal. While a full analysis of the intermolecular structure of the EP-PDI crystal edges is beyond the scope of this work, the images in **Figure 5** demonstrate the lock-in camera's ability to spatially resolve distinct excited state populations within a heterogeneous material and track their ensuing dynamics.

## Conclusions

In this work we have described the use of a lock-in camera for widefield transient

absorption imaging. We have detailed the triggering scheme to acquire $\Delta T$ and $T$ in the in-phase and quadrature channels of the camera. To demonstrate different imaging configurations, transient images of EP-PDI crystals were acquired with a widefield probe and two different configurations for the pump: focused and widefield excitation. The focused pump transients demonstrate the lock-in camera's capability to track the spatial distribution of photoexcited species as a function of time while the widefield pump transients demonstrate the lock-in camera's ability to correlate variations in the local structure of a material with its transient dynamics. For the organic crystals we investigate, we readily achieve widefield TAM images using the lock-in camera that possess signal-to-noise ratios that match those achieved using more expensive emCCD and sCMOS detectors by other groups. The lock-in camera can also provide additional advantages due to its ability to reach a 1 MHz frame rate that complements MHz fiber lasers currently available for ultrafast spectroscopy. This can in principle allow for shot-to-shot imaging. The lock-in camera also performs image subtraction and processing on board, freeing up memory resources on computers used for data acquisition. We anticipate that the lock-in imaging that we demonstrate here will enable new studies of the transport of photoexcited species and spatially-heterogeneous dynamics within a range of materials and chemical systems.

**Acknowledgements**

This work was supported by the Center for Adapting Flaws as Features under NSF Award CHE-2124983. TAM instrumentation employed for this work was produced via a NSF MRI development grant (CHE-2019083). STR and CB also acknowledge additional support from the Robert A. Welch Foundation (F-1885 to STR and F-1891 to CB). KSW acknowledges partial salary support from the Center for Dynamics and Control of Materials, a NSF MRSEC funded under grant DMR-2308817.

## Supporting Information Available

Detailed description of the laser setups used for TAM measurements. Description of the subtraction scheme used to suppress baseline drift within acquired camera images.

## References


(1) Piland, G.; Grumstrup, E. M. High-Repetition Rate Broadband Pump–Probe Microscopy. *J. Phys. Chem. A* **2019**, *123* (40), 8709–8716.

(2) Kanal, F.; Keiber, S.; Eck, R.; Brixner, T. 100-kHz Shot-to-Shot Broadband Data Acquisition for High-Repetition-Rate Pump–Probe Spectroscopy. *Opt. Express, OE* **2014**, *22* (14), 16965–16975. https://doi.org/10.1364/OE.22.016965.

(3) Kearns, N. M.; Mehlenbacher, R. D.; Jones, A. C.; Zanni, M. T. Broadband 2D Electronic Spectrometer Using White Light and Pulse Shaping: Noise and Signal Evaluation at 1 and 100 kHz. *Opt. Express, OE* **2017**, *25* (7), 7869–7883. https://doi.org/10.1364/OE.25.007869.

(4) Davydova, D.; Cadena, A. de la; Akimov, D.; Dietzek, B. Transient Absorption Microscopy: Advances in Chemical Imaging of Photoinduced Dynamics. *Laser & Photonics Reviews* **2016**, *10* (1), 62–81. https://doi.org/10.1002/lpor.201500181.

(5) Deng, S.; Blach, D. D.; Jin, L.; Huang, L. Imaging Carrier Dynamics and Transport in Hybrid Perovskites with Transient Absorption Microscopy. *Advanced Energy Materials* **2020**, *10* (26), 1903781. https://doi.org/10.1002/aenm.201903781.

(6) Dong, P.-T.; Cheng, J.-X. Pump–Probe Microscopy: Theory, Instrumentation, and Applications. *Spectroscopy Online* **2017**, *32* (4), 24–36.

(7) Zhu, Y.; Cheng, J.-X. Transient Absorption Microscopy: Technological Innovations and Applications in Materials Science and Life Science. *J. Chem. Phys.* **2020**, *152* (2), 020901. https://doi.org/10.1063/1.5129123.

(8) Gross, N.; Kuhs, C. T.; Ostovar, B.; Chiang, W.-Y.; Wilson, K. S.; Volek, T. S.; Faitz, Z. M.; Carlin, C. C.; Dionne, J. A.; Zanni, M. T.; et al. Progress and Prospects in Optical Ultrafast Microscopy in the Visible Spectral Region: Transient Absorption and Two-Dimensional Microscopy. *J. Phys. Chem. C* **2023**, *127* (30), 14557–14586. https://doi.org/10.1021/acs.jpcc.3c02091.

(9) Shi, H.; Yan, R.; Bertolazzi, S.; Brivio, J.; Gao, B.; Kis, A.; Jena, D.; Xing, H. G.; Huang, L. Exciton Dynamics in Suspended Monolayer and Few-Layer MoS2 2D Crystals. *ACS Nano* **2013**, *7* (2), 1072–1080. https://doi.org/10.1021/nn303973r.

(10) Williams, O. F.; Zhou, N.; Hu, J.; Ouyang, Z.; Kumbhar, A.; You, W.; Moran, A. M. Imaging Excited State Dynamics in Layered 2D Perovskites with Transient Absorption Microscopy. *J. Phys. Chem. A* **2019**, *123* (51), 11012–11021. https://doi.org/10.1021/acs.jpca.9b08852.

(11) Han, X.; Liang, X.; He, D.; Jiao, L.; Wang, Y.; Zhao, H. Photocarrier Dynamics in MoTe2 Nanofilms with 2H and Distorted 1T Lattice Structures. *ACS Appl. Mater. Interfaces* **2021**, *13* (37), 44703–44710. https://doi.org/10.1021/acsami.1c09698.

(12) Wang, P.; He, D.; He, J.; Fu, J.; Liu, S.; Han, X.; Wang, Y.; Zhao, H. Transient Absorption Microscopy of Layered Crystal AsSbS3. *J. Phys. Chem. A* **2020**, *124* (5), 1047–1052. https://doi.org/10.1021/acs.jpca.9b11940.

(13) Yoon, S. J.; Guo, Z.; dos Santos Claro, P. C.; Shevchenko, E. V.; Huang, L. Direct Imaging of Long-Range Exciton Transport in Quantum Dot Superlattices by Ultrafast Microscopy. *ACS Nano* **2016**, *10* (7), 7208–7215. https://doi.org/10.1021/acsnano.6b03700.

(14) Liu, M.; Verma, S. D.; Zhang, Z.; Sung, J.; Rao, A. Nonequilibrium Carrier Transport in Quantum Dot Heterostructures. *Nano Lett.* **2021**, *21* (21), 8945–8951. https://doi.org/10.1021/acs.nanolett.1c01892.

(15) Zhang, Z.; Sung, J.; Toolan, D. T. W.; Han, S.; Pandya, R.; Weir, M. P.; Xiao, J.; Dowland, S.; Liu, M.; Ryan, A. J.; et al. Ultrafast Exciton Transport at Early Times in Quantum Dot Solids. *Nat. Mater.* **2022**, *21* (5), 533–539. https://doi.org/10.1038/s41563-022-01204-6.

(16) Seo, M. A.; Yoo, J.; Dayeh, S. A.; Picraux, S. T.; Taylor, A. J.; Prasankumar, R. P. Mapping Carrier Diffusion in Single Silicon Core–Shell Nanowires with Ultrafast Optical Microscopy. *Nano Lett.* **2012**, *12* (12), 6334–6338. https://doi.org/10.1021/nl303502f.

(17) Folie, B. D.; Tan, J. A.; Huang, J.; Sercel, P. C.; Delor, M.; Lai, M.; Lyons, J. L.; Bernstein, N.; Efros, A. L.; Yang, P.; et al. Effect of Anisotropic Confinement on Electronic Structure and Dynamics of Band Edge Excitons in Inorganic Perovskite Nanowires. *J. Phys. Chem. A* **2020**, *124* (9), 1867–1876. https://doi.org/10.1021/acs.jpca.9b11981.

(18) Gabriel, M. M.; Kirschbrown, J. R.; Christesen, J. D.; Pinion, C. W.; Zigler, D. F.; Grumstrup, E. M.; Mehl, B. P.; Cating, E. E. M.; Cahoon, J. F.; Papanikolas, J. M. Direct Imaging of Free Carrier and Trap Carrier Motion in Silicon Nanowires by Spatially-Separated Femtosecond Pump–Probe Microscopy. *Nano Lett.* **2013**, *13* (3), 1336–1340. https://doi.org/10.1021/nl400265b.

(19) Wong, C. Y.; Cotts, B. L.; Wu, H.; Ginsberg, N. S. Exciton Dynamics Reveal Aggregates with Intermolecular Order at Hidden Interfaces in Solution-Cast Organic Semiconducting Films. *Nature Communications* **2015**, *6*, ncomms6946. https://doi.org/10.1038/ncomms6946.

(20) Zhu, T.; Huang, L. Exciton Transport in Singlet Fission Materials: A New Hare and Tortoise Story. *J. Phys. Chem. Lett.* **2018**, *9* (22), 6502–6510. https://doi.org/10.1021/acs.jpclett.8b02181.

(21) Zhu, T.; Wan, Y.; Huang, L. Direct Imaging of Frenkel Exciton Transport by Ultrafast Microscopy. *Acc. Chem. Res.* **2017**, *50* (7), 1725–1733. https://doi.org/10.1021/acs.accounts.7b00155.

(22) Ashoka, A.; Gauriot, N.; Girija, A. V.; Sawhney, N.; Sneyd, A. J.; Watanabe, K.; Taniguchi, T.; Sung, J.; Schnedermann, C.; Rao, A. Direct Observation of Ultrafast Singlet Exciton Fission in Three Dimensions. *Nat Commun* **2022**, *13* (1), 5963. https://doi.org/10.1038/s41467-022-33647-5.

(23) Schnedermann, C.; Sung, J.; Pandya, R.; Verma, S. D.; Chen, R. Y. S.; Gauriot, N.; Bretscher, H. M.; Kukura, P.; Rao, A. Ultrafast Tracking of Exciton and Charge Carrier Transport in Optoelectronic Materials on the Nanometer Scale. *J Phys Chem Lett* **2019**, *10* (21), 6727–6733. https://doi.org/10.1021/acs.jpclett.9b02437.

(24) Volek, T. S.; Armstrong, Z. T.; Sowa, J. K.; Wilson, K. S.; Bohlmann Kunz, M.; Bera, K.; Koble, M.; Frontiera, R. R.; Rossky, P. J.; Zanni, M. T.; et al. Structural Disorder at the Edges of Rubrene Crystals Enhances Singlet Fission. *J. Phys. Chem. Lett.* **2023**, 11497–11505. https://doi.org/10.1021/acs.jpclett.3c02845.

(25) Jones, A. C.; Kearns, N. M.; Ho, J.-J.; Flach, J. T.; Zanni, M. T. Impact of Non-Equilibrium Molecular Packings on Singlet Fission in Microcrystals Observed Using 2D White-Light Microscopy. *Nature Chemistry* **2019**, 1–8. https://doi.org/10.1038/s41557-019-0368-9.

(26) Kobayashi, T. Advanced Time-Resolved Absorption Spectroscopy with an Ultrashort Visible/near IR Laser and a Multi-Channel Lock-in Detector. *Proceedings of the Japan Academy, Series B* **2021**, *97* (5), 236–260. https://doi.org/10.2183/pjab.97.014.

(27) Kobayashi, T.; Du, J.; Feng, W.; Yoshino, K.; Tretiak, S.; Saxena, A.; Bishop, A. R. Observation of Breather Excitons and Soliton in a Substituted Polythiophene with a Degenerate Ground State. *Phys. Rev. B* **2010**, *81* (7), 075205. https://doi.org/10.1103/PhysRevB.81.075205.

(28) Salbut, L.; Pakuła, A.; Tomczewski, S.; Styk, A. Portable Profilometer Based on Low-Coherence Interferometry and Smart Pixel Camera. In *Speckle 2010: Optical Metrology*; SPIE, 2010; Vol. 7387, pp 331–337. https://doi.org/10.1117/12.871532.

(29) Meier, A. H.; Roesgen, T. Imaging Laser Doppler Velocimetry. *Exp Fluids* **2012**, *52* (4), 1017–1026. https://doi.org/10.1007/s00348-011-1192-1.

(30) Rangarajan, P.; Willomitzer, F.; Cossairt, O.; Christensen, M. P. Spatially Resolved Indirect Imaging of Objects beyond the Line of Sight. In *Unconventional and Indirect Imaging, Image Reconstruction, and Wavefront Sensing 2019*; SPIE, 2019; Vol. 11135, pp 124–131. https://doi.org/10.1117/12.2529001.

(31) Webb, J. L.; Troise, L.; Hansen, N. W.; Frellsen, L. F.; Osterkamp, C.; Jelezko, F.; Jankuhn, S.; Meijer, J.; Berg-Sørensen, K.; Perrier, J.-F.; Huck, A.; et al. High Speed Microcircuit and Synthetic Biosignal Widefield Imaging Using Nitrogen Vacancies in Diamond. *Phys. Rev. Applied* **2022**, *17* (6), 064051. https://doi.org/10.1103/PhysRevApplied.17.064051.

(32) Parashar, M.; Bathla, A.; Shishir, D.; Gokhale, A.; Bandyopadhyay, S.; Saha, K. Sub-Second Temporal Magnetic Field Microscopy Using Quantum Defects in Diamond. *Sci Rep* **2022**, *12* (1), 8743. https://doi.org/10.1038/s41598-022-12609-3.

(33) Seo, M.; Boubanga-Tombet, S.; Yoo, J.; Ku, Z.; Gin, A. V.; Picraux, S. T.; Brueck, S. R. J.; Taylor, A. J.; Prasankumar, R. P. Ultrafast Optical Wide Field Microscopy. *Opt. Express, OE* **2013**, *21* (7), 8763–8772. https://doi.org/10.1364/OE.21.008763.

(34) Le, A. K.; Bender, J. A.; Arias, D. H.; Cotton, D. E.; Johnson, J. C.; Roberts, S. T. Singlet Fission Involves an Interplay between Energetic Driving Force and Electronic Coupling in Perylenediimide Films. *J. Am. Chem. Soc.* **2018**, *140* (2), 814–826. https://doi.org/10.1021/jacs.7b11888.

(35) Aulin, Y. V.; Felter, K. M.; Günbas, D. D.; Dubey, R. K.; Jager, W. F.; Grozema, F. C. Morphology-Independent Efficient Singlet Exciton Fission in Perylene Diimide Thin Films. *ChemPlusChem* **2018**, *83* (4), 230–238. https://doi.org/10.1002/cplu.201700449.

(36) Murugan, P.; Ravindran, E.; Sangeetha, V.; Liu, S.-Y.; Woong Jung, J. Perylene-Diimide for Organic Solar Cells: Current Scenario and Prospects in Molecular Geometric, Functionalization, and Optoelectronic Properties. *Journal of Materials Chemistry A* **2023**. https://doi.org/10.1039/D3TA04925F.

(37) Kim, Y.-J.; Lee, Y.; Park, K.; Ahn, C. W.; Jung, H.-T.; Jeon, H.-J. Hierarchical Self-Assembly of Perylene Diimide (PDI) Crystals. 10.

(38) Delor, M.; Weaver, H. L.; Yu, Q.; Ginsberg, N. S. Imaging Material Functionality through Three-Dimensional Nanoscale Tracking of Energy Flow. *Nature Materials* **2020**, *19* (1), 56–62. https://doi.org/10.1038/s41563-019-0498-x.

(39) Guo, Z.; Manser, J. S.; Wan, Y.; Kamat, P. V.; Huang, L. Spatial and Temporal Imaging of Long-Range Charge Transport in Perovskite Thin Films by Ultrafast Microscopy. *Nature Communications* **2015**, *6* (1), 7471. https://doi.org/10.1038/ncomms8471.

(40) Thiebes, J. J.; Grumstrup, E. M. Quantifying Noise Effects in Optical Measures of Excited State Transport. *The Journal of Chemical Physics* **2024**, *160* (12), 124201. https://doi.org/10.1063/5.0190347.

(41) Zhu, T.; Snaider, J. M.; Yuan, L.; Huang, L. Ultrafast Dynamic Microscopy of Carrier and Exciton Transport. *Annual Review of Physical Chemistry* **2019**, *70* (1), 219–244. https://doi.org/10.1146/annurev-physchem-042018-052605.

(42) Ginsberg, N. S.; Tisdale, W. A. Spatially Resolved Photogenerated Exciton and Charge Transport in Emerging Semiconductors. *Annual Review of Physical Chemistry* **2020**, *71* (1), 1–30. https://doi.org/10.1146/annurev-physchem-052516-050703.

(43) Berghuis, A. M.; Raziman, T. V.; Halpin, A.; Wang, S.; Curto, A. G.; Rivas, J. G. Effective Negative Diffusion of Singlet Excitons in Organic Semiconductors. *J. Phys. Chem. Lett.* **2021**, *12* (4), 1360–1366. https://doi.org/10.1021/acs.jpclett.0c03171.

(44) Firdaus, Y.; Le Corre, V. M.; Karuthedath, S.; Liu, W.; Markina, A.; Huang, W.; Chattopadhyay, S.; Nahid, M. M.; Nugraha, M. I.; Lin, Y.; et al. Long-Range Exciton Diffusion in Molecular Non-Fullerene Acceptors. *Nat Commun* **2020**, *11* (1), 5220. https://doi.org/10.1038/s41467-020-19029-9.

(45) Adhyaksa, G. W. P.; Brittman, S.; Āboliņš, H.; Lof, A.; Li, X.; Keelor, J. D.; Luo, Y.; Duevski, T.; Heeren, R. M. A.; Ellis, S. R.; et al. Understanding Detrimental and Beneficial Grain Boundary Effects in Halide Perovskites. *Advanced Materials* **2018**, *30* (52), 1804792. https://doi.org/10.1002/adma.201804792.

(46) Gegevičius, R.; Franckevičius, M.; Gulbinas, V. The Role of Grain Boundaries in Charge Carrier Dynamics in Polycrystalline Metal Halide Perovskites. *European Journal of Inorganic Chemistry* **2021**, *2021* (35), 3519–3527. https://doi.org/10.1002/ejic.202100360.

(47) Huo, Y.; Li, Z.; Zhang, J.; Dai, K.; Liang, C.; Yang, Y. Defect-Mediated Electron–Hole Separation in an Inorganic–Organic CdSxSe1−x–DETA Solid Solution under Amine Molecule-Assisted Fabrication and Microwave-Assisted Method for Promoting Photocatalytic H2 Evolution. *Sustainable Energy Fuels* **2019**, *3* (12), 3550–3560. https://doi.org/10.1039/C9SE00633H.

(48) Khassaf, H.; Yadavalli, S. K.; Zhou, Y.; Padture, N. P.; Kingon, A. I. Effect of Grain Boundaries on Charge Transport in Methylammonium Lead Iodide Perovskite Thin Films. *J. Phys. Chem. C* **2019**, *123* (9), 5321–5325. https://doi.org/10.1021/acs.jpcc.9b00538.

(49) Sarkar, R.; Kar, M.; Habib, M.; Zhou, G.; Frauenheim, T.; Sarkar, P.; Pal, S.; Prezhdo, O. V. Common Defects Accelerate Charge Separation and Reduce Recombination in CNT/Molecule Composites: Atomistic Quantum Dynamics. *J. Am. Chem. Soc.* **2021**, *143* (17), 6649–6656. https://doi.org/10.1021/jacs.1c02325.

(50) Pandya, R.; Chen, R. Y. S.; Gu, Q.; Gorman, J.; Auras, F.; Sung, J.; Friend, R.; Kukura, P.; Schnedermann, C.; Rao, A. Femtosecond Transient Absorption Microscopy of Singlet Exciton Motion in Side-Chain Engineered Perylene-Diimide Thin Films. *J. Phys. Chem. A* **2020**, *124* (13), 2721–2730. https://doi.org/10.1021/acs.jpca.0c00346.

(51) Liu, X.; Xu, H.; Zhou, Y.; Yang, C.; Liu, G.; Luo, L.; Wang, W.; Ma, Y.; Jin, J.; Zhang, J.; et al. Solution-Processed Self-Assemble Engineering PDI Derivative Polymorphisms with Optoelectrical Property Tuning in Organic Field-Effect Transistors. *Organic Electronics* **2020**, *83*, 105777. https://doi.org/10.1016/j.orgel.2020.105777.

**TOC Graphic**

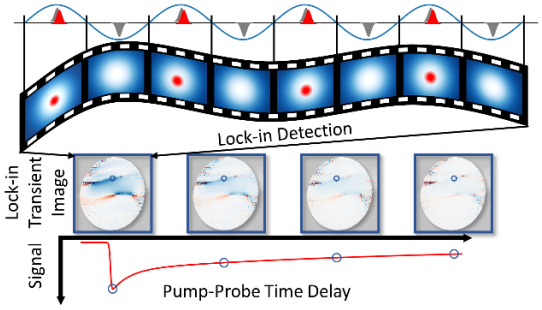
Lock-in Detection
Lock-in Transient Image
Signal
Pump-Probe Time Delay